





Cite this: *Phys. Chem. Chem. Phys.*,  
2024, 26, 3950

# Doping SnO<sub>2</sub> with metal ions of varying valence states: discerning the importance of active surface oxygen species vs. acid sites for C<sub>3</sub>H<sub>8</sub> and CO oxidation†

Haiming Yan, Teng Liu, Yu Lv, Xianglan Xu,  Junwei Xu, Xiuzhong Fang and Xiang Wang \*

To elucidate the valence state effect of doping cations, Li<sup>+</sup>, Mg<sup>2+</sup>, Cr<sup>3+</sup>, Zr<sup>4+</sup> and Nb<sup>5+</sup> with radii similar to Sn<sup>4+</sup> (CN = 6) were chosen to dope tetragonal SnO<sub>2</sub>. Cr<sup>3+</sup>, Zr<sup>4+</sup> and Nb<sup>5+</sup> can enter the SnO<sub>2</sub> lattice to produce solid solutions, thus creating more surface defects. However, Li<sup>+</sup> and Mg<sup>2+</sup> can only stay on the SnO<sub>2</sub> surface as nitrates, thus suppressing the surface defects. The rich surface defects facilitate the generation of active O<sub>2</sub><sup>−</sup>/O<sup>δ−</sup> and acid sites on the solid solution catalysts, hence improving the reactivity. On the solid solution catalysts active for propane combustion, several reactive intermediates can be formed, but are negligible on those with low activity. It is confirmed that for propane combustion, surface acid sites play a more vital role than active oxygen sites. Nevertheless, for CO oxidation, the active oxygen sites play a more vital role than the acid sites.

Received 30th November 2023,  
Accepted 9th January 2024

DOI: 10.1039/d3cp05840a

rsc.li/pccp

## 1. Introduction

Rapid global industrialization has led to the release of a large amount of volatile organic compounds (VOCs) into the atmosphere, which poses not only environmental problems but also various threats to human health.<sup>1–4</sup> Therefore, the abatement of VOCs is one of the compelling global challenges faced by every country. Catalytic combustion stands out as one of the most promising methods for effectively eliminating these pollutants.<sup>5–9</sup> Catalysts containing noble metals, such as Pt, Pd, Ru *etc.*, exhibit high activity for VOC combustion.<sup>10–14</sup> However, the widespread application of noble metals has been restricted due to their high cost.<sup>5,15,16</sup> The development of non-noble metal catalysts has considerable advantages because of their cost-effectiveness and greater availability of resources, which has received considerable attention from researchers in recent decades.<sup>17–20</sup>

Due to its abundant lattice and surface defects/vacancies, tetragonal rutile SnO<sub>2</sub>, as an n-type semiconducting oxide, finds applications in gas sensors, solar cells, semiconductor devices, and electrode materials.<sup>21–23</sup> Previous investigations have validated that the surface defect enables the adsorption

and activation of gaseous O<sub>2</sub>, thus resulting in the generation of abundant active O<sub>2</sub><sup>−</sup> and O<sub>2</sub><sup>2−</sup> sites,<sup>24–26</sup> whereas these surface oxygen species on pure SnO<sub>2</sub> can be relinquished when calcined at temperatures exceeding 300 °C, which thus limits its redox property and reactivity.<sup>27,28</sup> The incorporation of secondary metal ions in the SnO<sub>2</sub> matrix has been reported to effectively stabilize the surface-active oxygen sites. For example, former studies have demonstrated that the introduction of Cu<sup>2+</sup>, Fe<sup>3+</sup>, Cr<sup>3+</sup>, Ta<sup>5+</sup>, Ce<sup>4+</sup> and Nb<sup>5+</sup> in the SnO<sub>2</sub> lattice to form solid solutions not only improves the concentration of active surface oxygen sites but also stabilizes them at temperatures higher than 300 °C, due to the formation of more lattice/surface defects and charge imbalance.<sup>28–33</sup>

The utilization of solid solutions with diverse chemical compositions is crucial for a wide range of catalytic reactions, and has gained significant attention.<sup>16,34</sup> As indicated by previous investigations, the formation of steady solid solutions can only be achieved if the two cations possess similar radii and electronegativities.<sup>35,36</sup> The additive materials alter the bulk structure and surface defects of the host matrix, which depends on their ionic radii and valence states.

Nevertheless, the effect of doping ions with varied valence states on the structure and reactivity of solid solution catalysts has not yet been investigated systematically. Researchers still lack clear understanding of some important fundamental scientific issues. Aiming to resolve this problem, Li<sup>+</sup>, Mg<sup>2+</sup>, Cr<sup>3+</sup>, Zr<sup>4+</sup> and Nb<sup>5+</sup> cations with different valence states but having radii similar to Sn<sup>4+</sup> have been selected to modify SnO<sub>2</sub>

Key Laboratory of Jiangxi Province for Environment and Energy Catalysis, School of Chemistry and Chemical Engineering, Nanchang University, Nanchang, Jiangxi, 330031, P.R. China. E-mail: xwang23@ncu.edu.cn

† Electronic supplementary information (ESI) available. See DOI: <https://doi.org/10.1039/d3cp05840a>

by using a sol-gel method, with the expectation to incorporate them into the lattice of  $\text{SnO}_2$  to obtain solid solutions. The prepared catalysts are tested *via* CO and propane oxidation to elucidate their surface-active sites and reactivity from different angles. Indeed, it was discovered that while  $\text{Cr}^{3+}$ ,  $\text{Zr}^{4+}$  and  $\text{Nb}^{5+}$  can be successfully doped in the  $\text{SnO}_2$  matrix to achieve solid solutions,  $\text{Li}^+$  and  $\text{Mg}^{2+}$  cannot enter the  $\text{SnO}_2$  lattice because the valence state deviation is too large. Moreover, we found that for CO oxidation, the active surface oxygen sites play a more critical role than the surface acid sites. However, for propane oxidation, the surface acid sites play a more crucial role than the active surface oxygen sites.

## 2. Experimental section

### 2.1 Catalyst preparation

The samples were fabricated using a sol-gel method. The detailed preparation process is outlined in the ESI.†

### 2.2 Catalyst characterization and activity testing

The samples were characterized by X-ray diffraction (XRD), Raman Spectroscopy, X-ray photoelectron spectroscopy (XPS),

$\text{H}_2$  temperature programmed reduction ( $\text{H}_2$ -TPR),  $\text{O}_2$  temperature programmed desorption ( $\text{O}_2$ -TPD),  $\text{NH}_3$  temperature programmed desorption ( $\text{NH}_3$ -TPD), propane temperature programmed desorption (propane-TPD), electron paramagnetic resonance (EPR), high resolution transmission electron microscope (HRTEM), scanning transmission electron microscopy-mapping (STEM-mapping) and *in situ* DRIFTS techniques. The catalytic performance was assessed through CO oxidation and propane combustion. Notably, to get reliable and useful reaction kinetic data to guide catalyst design, the reaction feeds simulate real after-treatment processes by using air as an oxidant, which consists of  $\sim 78\%$   $\text{N}_2$  and  $21\%$   $\text{O}_2$ . The equipment models, experimental procedures, reaction conditions and operation parameters are described in the ESI.†

## 3. Results and discussion

### 3.1 XRD and Raman analysis

The XRD patterns are manifested in Fig. 1(a) for the catalysts, and the quantification results are listed in Table 1. Three strongest peaks around  $26.3^\circ$  (110),  $33.6^\circ$  (101) and  $51.5^\circ$  (211), which are characteristic of tetragonal rutile  $\text{SnO}_2$ , are observed for all the samples,<sup>24</sup> but with varied intensity. The lattice parameters of the samples, as presented in Table 1, exhibit a remarkable resemblance to those of the individual  $\text{SnO}_2$ , thereby substantiating the retention of the tetragonal rutile structure. The absence of any peak associated with the dopant cations suggests their possible incorporation into the  $\text{SnO}_2$  lattice to produce solid solutions, or their high dispersion on the surface of  $\text{SnO}_2$ , thereby evading detection *via* XRD.

Theoretically, to effectively establish a solid solution between two metal oxides, the two metal cations must have a similar radius and electronegativity.<sup>31,35</sup> The  $\text{Sn}^{4+}$  cations in rutile  $\text{SnO}_2$  have a coordination number (CN) of 6 and possess an ionic radius of  $0.69 \text{ \AA}$ . The XPS analysis in this study has confirmed the predominant presence of the doping metal cations such as  $\text{Li}^+$ ,  $\text{Mg}^{2+}$ ,  $\text{Cr}^{3+}$ ,  $\text{Zr}^{4+}$  and  $\text{Nb}^{5+}$ . Further details of these findings will be described in the XPS section. If these cations possess a CN of 6, their radii will be  $0.76$ ,  $0.72$ ,  $0.62$ ,  $0.72$  and  $0.64 \text{ \AA}$ , respectively, which are similar to that of  $\text{Sn}^{4+}$ . According to the basic requirement, it is theoretically feasible to generate stable solid solutions between  $\text{SnO}_2$  and these cations, whereas the valence states of all cations differ from  $\text{Sn}^{4+}$  except for  $\text{Zr}^{4+}$ , thus potentially affecting the generation of a solid solution structure.

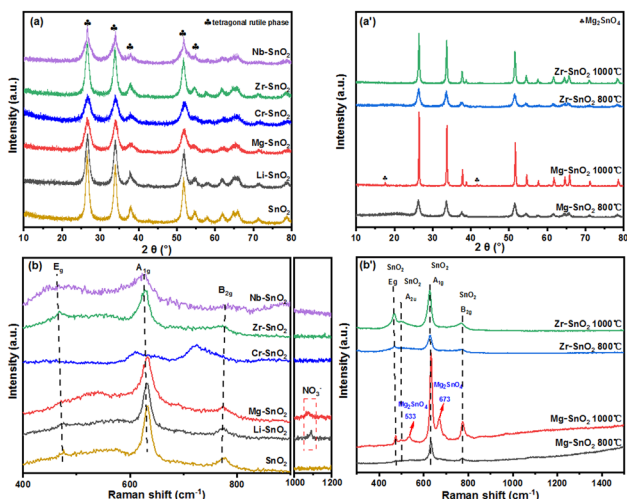


Fig. 1 Structural identification of the catalysts. (a) XRD patterns of the catalysts calcined at  $500^\circ\text{C}$ ; (a') XRD patterns of  $\text{Mg-SnO}_2$  and  $\text{Zr-SnO}_2$  calcined at  $800^\circ\text{C}$  and  $1000^\circ\text{C}$ ; (b) Raman spectra of the catalysts calcined at  $500^\circ\text{C}$ ; (b') Raman spectra of  $\text{Mg-SnO}_2$  and  $\text{Zr-SnO}_2$  calcined at  $800^\circ\text{C}$  and  $1000^\circ\text{C}$ .

Table 1 The physicochemical properties

Catalysts	Coordination number (CN)	Dopant ionic radius ( $\text{\AA}$ )	Sn/M molar ratio <sup>a</sup>	Lattice parameters			Average crystallite size <sup>b</sup> (nm)	Average grain size <sup>c</sup>	Surface area ( $\text{m}^2 \text{g}^{-1}$ )
				$a = b$ ( $\text{\AA}$ )	$c$ ( $\text{\AA}$ )	$\alpha = \beta = \gamma$ ( $^\circ$ )			
$\text{SnO}_2$	6	0.69	—	4.806	3.211	90	7.2	—	24.2
$\text{Li-SnO}_2$	6	0.76	8.0/1	4.778	3.225	90	6.9	—	26.8
$\text{Mg-SnO}_2$	6	0.72	7.0/1	4.746	3.210	90	4.8	4.9	42.6
$\text{Cr-SnO}_2$	6	0.62	8.9/1	4.767	3.201	90	5.4	5.8	40.5
$\text{Zr-SnO}_2$	6	0.72	9.0/1	4.810	3.212	90	6.1	6.2	30.7
$\text{Nb-SnO}_2$	6	0.64	9.0/1	4.796	3.206	90	5.8	6.1	32.3

<sup>a</sup> Measured *via* ICP. <sup>b</sup> Calculated using the Scherrer equation with the XRD (110) peak of  $\text{SnO}_2$ . <sup>c</sup> Measured *via* HRTEM.

Hence, the catalysts were subjected to Raman analysis for further clarification. The Raman spectra of pure  $\text{SnO}_2$ , as illustrated in Fig. 1(b), exhibit an  $E_g$  peak at  $476\text{ cm}^{-1}$ , a prominent  $A_{1g}$  peak at  $633\text{ cm}^{-1}$ , and a minor  $B_{2g}$  peak at  $775\text{ cm}^{-1}$ .<sup>25</sup> Analogously, all the modified catalysts also show these three typical Raman bands, confirming that  $\text{SnO}_2$  could still be in the crystalline phase. However, the  $E_g$ ,  $A_{1g}$  and  $B_{2g}$  peaks of  $\text{Cr}^{3+}$ ,  $\text{Zr}^{4+}$  and  $\text{Nb}^{5+}$ -doped samples are shifted and broadened in contrast to those of pure  $\text{SnO}_2$ , which may be attributed to variations in the  $\text{SnO}_2$  lattice parameters and the presence of surface vacancies/defects resulting from a solid solution structure.<sup>30</sup> In contrast, the samples doped by  $\text{Li}^+$  and  $\text{Mg}^{2+}$  show spectra similar to that of individual  $\text{SnO}_2$  without evident peak shift and broadening, and a characteristic peak of nitrate was observed around  $1075\text{ cm}^{-1}$ .<sup>37</sup> This suggests the presence of  $\text{Li}^+$  and  $\text{Mg}^{2+}$  on the surface of  $\text{SnO}_2$  as nitrates rather than their incorporation into its matrix to produce a solid solution structure. Although  $\text{Li}^+$  and  $\text{Mg}^{2+}$  have radii similar to that of  $\text{Sn}^{4+}$ , their valence states are very different from that of  $\text{Sn}^{4+}$ , which may result in too big difference in electronegativity to generate a solid solution structure.

To validate this further,  $\text{Mg-SnO}_2$  and  $\text{Zr-SnO}_2$ , the two typical samples, were calcined at higher temperatures of 800 and 1000 °C, and analysed *via* XRD and Raman spectroscopy. As depicted in Fig. 1(a'), the tetragonal rutile  $\text{SnO}_2$  phase remains the sole crystalline phase for  $\text{Zr-SnO}_2$ , providing evidence for the generation of a stable solid solution structure, whereas for the  $\text{Mg-SnO}_2$  sample, when being calcined at 1000 °C, a new  $\text{Mg}_2\text{SnO}_4$  phase appears, accompanying the disappearance of the surface  $\text{Mg}(\text{NO}_3)_2$  species, which is also confirmed by the Raman results shown in Fig. 1(b'). This testifies again that for the Mg-doped samples,  $\text{Mg}(\text{NO}_3)_2$  is present on its surface rather than being incorporated into the matrix of  $\text{SnO}_2$ . Without the restriction of the crystal lattice,  $\text{Mg}(\text{NO}_3)_2$  reacted with  $\text{SnO}_2$  at high temperature to produce the  $\text{Mg}_2\text{SnO}_4$  compound.<sup>38</sup> Indeed, this has confirmed that  $\text{Cr}^{3+}$ ,  $\text{Zr}^{4+}$  and  $\text{Nb}^{5+}$  are incorporated into the lattice of tetragonal  $\text{SnO}_2$  to form solid solutions, while  $\text{Mg}^{2+}$  and  $\text{Li}^+$  are present on the surface as nitrates.

All the modified samples exhibit larger surface areas and smaller crystallite sizes than pure  $\text{SnO}_2$  (Table 1). The solid solution structure typically hinders the crystallization of materials due to disparities in radius and charge distribution.<sup>29,39</sup> Therefore, it is not difficult to understand that  $\text{Cr-SnO}_2$ ,  $\text{Zr-SnO}_2$  and  $\text{Nb-SnO}_2$  have improved surface areas. For  $\text{Li-SnO}_2$  and  $\text{Mg-SnO}_2$ , although a solid solution structure is not formed, the dispersion of Li and Mg nitrates on the surface can also hinder the crystallization process, thereby resulting in improved surface areas.<sup>40</sup>

### 3.2 TEM, HRTEM and STEM-mapping results

The morphologies, grain sizes, crystallite growth, and elemental distribution of some representative catalysts have been analysed using TEM and HRTEM and STEM-mapping techniques. In Fig. 2, the TEM images reveal that the samples consist of irregular spherical grains with average sizes comparable to their corresponding crystallite sizes, providing evidence that there is no

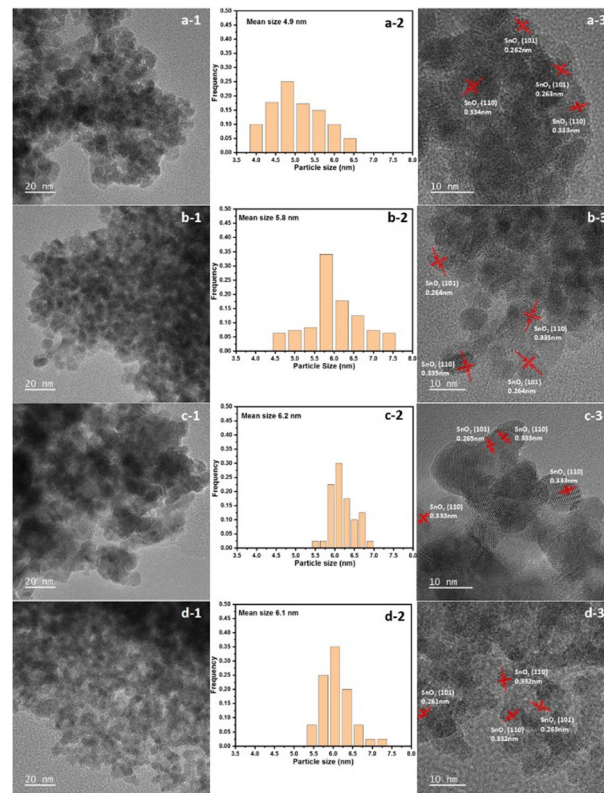


Fig. 2 HRTEM images and particle size distribution profiles: (a)  $\text{Mg-SnO}_2$ ; (b)  $\text{Cr-SnO}_2$ ; (c)  $\text{Zr-SnO}_2$ ; (d)  $\text{Nb-SnO}_2$ .

secondary agglomeration of the crystallites. The HRTEM images in Fig. 2 demonstrate that (110) and (101) diffraction planes of the  $\text{SnO}_2$  phase were detected distinctly for all the samples, but no crystalline phases related to the dopant oxides can be detected. This proves that for the solid solution samples, the dopant cations are substituted into the matrix, and for the samples without a solid solution structure, the dopant cations are dispersed finely on the surface as nitrates, as testified by Raman results.

The STEM-mapping images in Fig. 3 reveal a nearly uniform distribution of Sn, M, and O across all the samples, further supporting the presence of  $\text{Cr}^{3+}$ ,  $\text{Zr}^{4+}$  and  $\text{Nb}^{5+}$  in the  $\text{SnO}_2$  matrix to generate stable solid solutions, but  $\text{Mg}^{2+}$  stays on the surface of  $\text{SnO}_2$  in the form of highly dispersed nitrate.

### 3.3 Activity tests

To investigate the impact of different dopants on catalytic activity, we have conducted tests on the catalysts for CO and propane oxidation. Notably,  $\text{CO}_2$  is the only product detected for both reactions in the tested temperature region. The individual  $\text{SnO}_2$  exhibits certain activity, as shown in Fig. 4(a), due to the existence of active surface deficient oxygen and lattice oxygen species, on which CO is completely oxidized at 340 °C. It should be noted that  $\text{Cr}^{3+}$  and  $\text{Nb}^{5+}$  doping improves the activity, and the activity of  $\text{Zr-SnO}_2$  is close to that of pure  $\text{SnO}_2$ . In contrast,  $\text{Li}^+$  and  $\text{Mg}^{2+}$  doping clearly degrades the activity, on which 100% CO conversion is achieved at 410 °C and 420 °C,



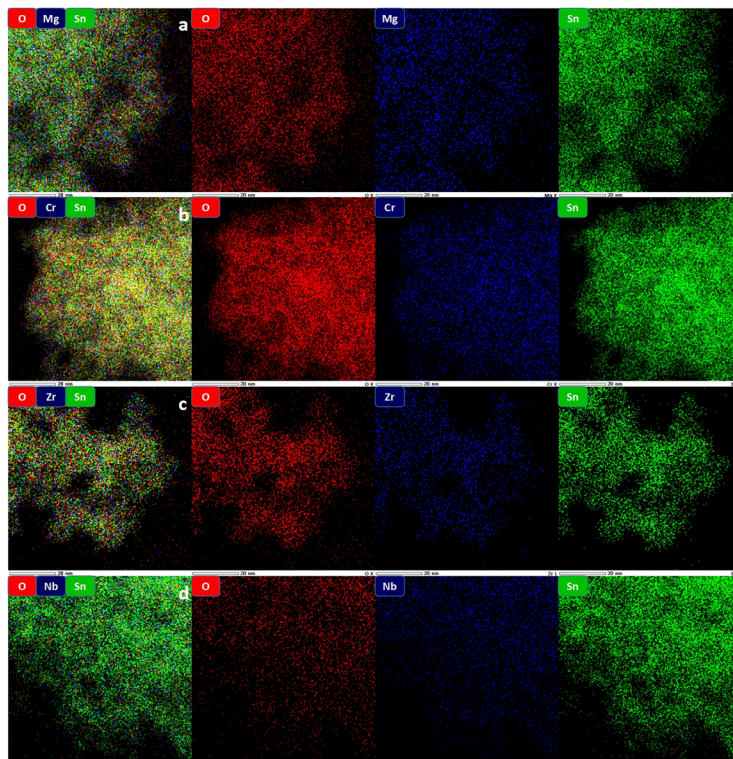


Fig. 3 STEM-mapping images of the catalysts: (a) Mg-SnO<sub>2</sub>; (b) Cr-SnO<sub>2</sub>; (c) Zr-SnO<sub>2</sub>; (d) Nb-SnO<sub>2</sub>.

respectively. Among all the catalysts, Nb-SnO<sub>2</sub> shows the highest activity, which can oxidize CO completely at 280 °C.

Arrhenius curves obtained under differential conditions are shown in Fig. 4(b). For clarity, Table 2 lists the CO conversion

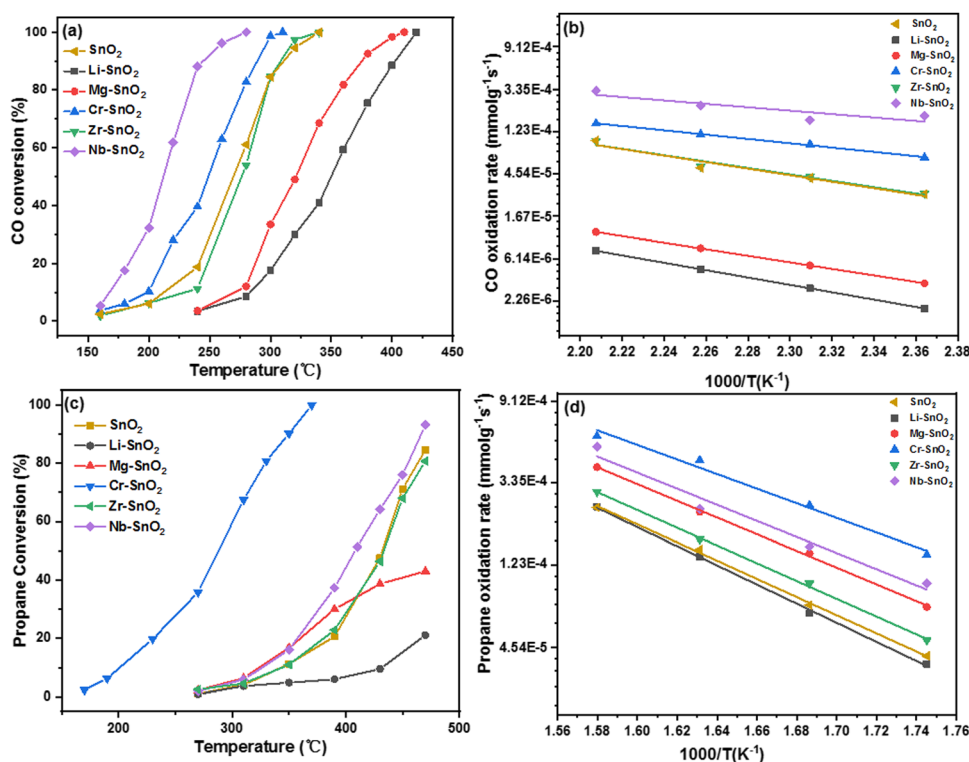


Fig. 4 CO and propane oxidation performance on the catalysts. (a) CO conversion; (b) Arrhenius plots for CO conversion; (c) propane conversion; (d) Arrhenius plots for propane conversion.

Table 2 CO and propane oxidation activity over M-SnO<sub>2</sub> catalysts

Samples	$R_w^a$ ( $10^{-5}$ mmol g <sup>-1</sup> s <sup>-1</sup> )		$R_s^b$ ( $10^{-6}$ mmol s <sup>-1</sup> m <sup>-2</sup> )		$E_a$ (kJ mol <sup>-1</sup> )	
	CO	Propane	CO	Propane	CO	Propane
SnO <sub>2</sub>	2.81	4.08	1.16	1.67	64.2	92.1
Li-SnO <sub>2</sub>	0.74	3.70	0.28	1.38	72.4	96.9
Mg-SnO <sub>2</sub>	1.15	7.43	0.27	1.59	64.2	84.7
Cr-SnO <sub>2</sub>	15.00	14.00	3.69	3.46	42.5	74.0
Zr-SnO <sub>2</sub>	2.86	4.93	0.93	1.66	62.8	90.0
Nb-SnO <sub>2</sub>	32.32	9.92	10.00	3.07	36.9	81.6

<sup>a</sup>  $R_w$ , the differential rates normalized by catalyst weight. Measured at 180 °C for CO oxidation and at 300 °C for propane combustion. <sup>b</sup>  $R_s$ , the differential rates normalized by catalyst surface area. Measured at 180 °C for CO oxidation and at 300 °C for propane combustion.

rates measured at 180 °C, that is,  $R_w$  and  $R_s$  normalized by catalyst weight and surface area, and the apparent activation energies. The reaction rates display a comparable trend to the overall activity, which is sequenced as Nb-SnO<sub>2</sub> > Cr-SnO<sub>2</sub> > Zr-SnO<sub>2</sub> ≈ SnO<sub>2</sub> > Mg-SnO<sub>2</sub> > Li-SnO<sub>2</sub>. Compared to pure SnO<sub>2</sub>, Nb-SnO<sub>2</sub> and Cr-SnO<sub>2</sub> have higher reaction rates and lower activation energy, which suggests that the incorporation of Nb<sup>5+</sup> and Cr<sup>3+</sup> into the solid solution structure leads to the formation of a greater number of active surface sites for CO oxidation. Previous studies have demonstrated that active surface oxygen species play a key role in CO oxidation reactions.<sup>41–43</sup> The formation of solid solutions leads to an increased abundance of surface vacancies, thereby promoting the creation of additional reactive oxygen sites on the surface and facilitating CO oxidation.<sup>44,45</sup> However, the presence of Li and Mg nitrates on the SnO<sub>2</sub> surface is obviously harmful to the activity.

Interestingly, the results in Fig. 4(c) and (d) demonstrate that the sequence of both overall and intrinsic activity for propane deep oxidation differs from that observed in CO oxidation. The overall activity is sequenced as Cr-SnO<sub>2</sub> > Nb-SnO<sub>2</sub> > Zr-SnO<sub>2</sub> ≈ SnO<sub>2</sub> > Mg-SnO<sub>2</sub> > Li-SnO<sub>2</sub>. Basically, the intrinsic activity judged by  $R_s$  obeys the same sequence. Cr-SnO<sub>2</sub> shows much higher activity than Nb-SnO<sub>2</sub> and other catalysts, which suggests that for propane deep oxidation, the surface acid sites might play a more vital role than the active

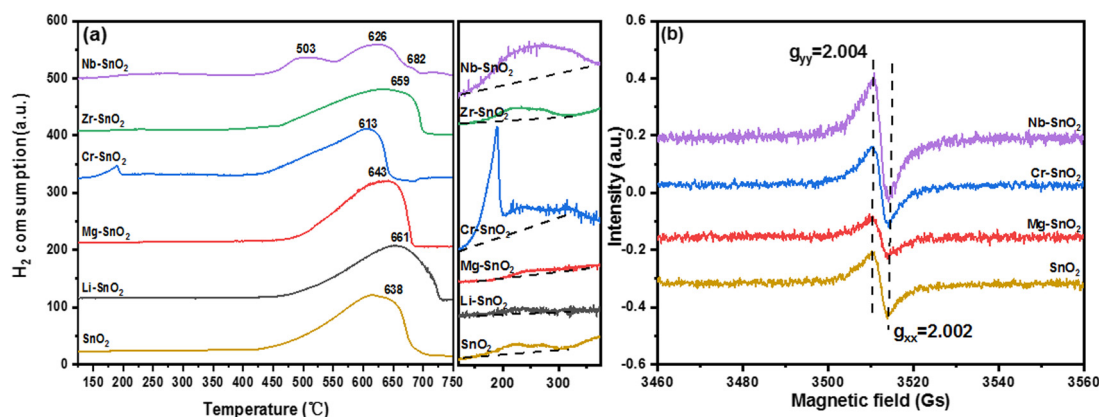
oxygen species. Therefore, it is proposed that surface acid sites could play a more critical role here, which can adsorb and activate those organic molecules with rich electrons, such as propane molecules in this work.<sup>46,47</sup>

### 3.4 H<sub>2</sub>-TPR, O<sub>2</sub>-TPD and EPR studies

To examine the impact of introducing different valence state ions, the redox properties were tested by conducting H<sub>2</sub>-TPR. As depicted in Fig. 5(a), the reduction peaks of all samples can be categorized into two distinct groups: one group ranging from 150 to 350 °C, and another group above 400 °C. The minor peak observed at 150–300 °C can be ascribed to the reduction of surface deficiency oxygen, which is typical for SnO<sub>2</sub> and related to its n-type semiconducting property,<sup>28,39</sup> whereas this facile oxygen species will be depleted on individual SnO<sub>2</sub> when the treating temperature exceeds 400 °C.<sup>27,28</sup> As manifested by the partly enlarged profiles beside the main figure and the quantification results in Table 3, the formation of the solid solution can significantly enhance the concentration of this active oxygen species and stabilize it at elevated temperature, especially for Cr-SnO<sub>2</sub> and Nb-SnO<sub>2</sub>. In contrast, for Li-SnO<sub>2</sub> and Mg-SnO<sub>2</sub> with the formation of Li and Mg nitrates on the surface, the concentration of this deficiency oxygen species decreases evidently, in good accordance with the CO oxidation activity sequence. This has proven that the surface deficient oxygen plays a crucial role for CO oxidation, although it is also necessary for propane deep oxidation.

Table 3 Quantified H<sub>2</sub>-TPR and O<sub>2</sub>-TPD results

Catalysts	H <sub>2</sub> uptake amount (mmol g <sup>-1</sup> )		O/Sn atomic ratio	O <sub>2</sub> desorption amount (μmol g <sup>-1</sup> )		
	Below 350 °C	Above 350 °C		α	β	α + β
SnO <sub>2</sub>	0.14	13.27	2.0	0.62	36.86	37.48
Li-SnO <sub>2</sub>	0.06	12.67	2.1	0.37	31.83	32.20
Mg-SnO <sub>2</sub>	0.05	12.11	2.0	0.47	35.41	35.88
Cr-SnO <sub>2</sub>	0.63	11.13	1.9	2.66	36.84	39.50
Zr-SnO <sub>2</sub>	0.18	11.81	2.0	0.60	37.17	37.77
Nb-SnO <sub>2</sub>	0.80	11.62	2.0	3.08	38.65	41.73

Fig. 5 (a) H<sub>2</sub>-TPR profiles of the catalysts; (b) EPR spectra of some typical catalysts.

EPR experiments were thus carried out using some typical samples to identify the facile oxygen species. The catalysts exhibit two bands at  $g = 2.004$  and  $2.002$ , as depicted in Fig. 5(b), which are assignable to surface  $\text{O}_2^-$ .<sup>48</sup> The order of the peak integrated areas is as follows,  $\text{Nb-SnO}_2 > \text{Cr-SnO}_2 > \text{SnO}_2 > \text{Mg-SnO}_2$ , in agreement with the CO oxidation activity sequence. The existence of surface  $\text{O}_2^-$  suggests that it may serve as one of the significant oxygen centres for CO oxidation.

The broad and significant reduction peak above  $400^\circ\text{C}$  can be attributed to the reduction of  $\text{Sn}^{4+}$  to  $\text{Sn}^0$ ,<sup>24,25</sup> which is further validated by the O/Sn molar ratio around 2 as shown in Table 3. With the doping of  $\text{Nb}^{5+}$  and  $\text{Cr}^{3+}$  to form solid solutions, the mobility of the lattice oxygen is obviously increased, thus becoming easier to be reduced.

The oxygen characteristics of the catalysts have been analysed from different perspectives using  $\text{O}_2$ -TPD. The desorption peaks observed in Fig. S1 (ESI<sup>†</sup>) can be categorized into two groups: one group, denoted as  $\alpha$  type, occurs in the temperature range of  $50$ – $200^\circ\text{C}$  and corresponds to the release of loosely bonded surface oxygen,<sup>24,49</sup> while the other group, referred as  $\beta$  type, appears between  $200$  and  $700^\circ\text{C}$  and is associated with the release of surface lattice  $\text{O}^{2-}$ .<sup>24,49</sup> As quantified in Table 3, the integrated areas of the  $\alpha$  peak for  $\text{Cr-SnO}_2$  and  $\text{Nb-SnO}_2$  show significant improvement, indicating the presence of a larger amount of surface facile oxygen compared to individual  $\text{SnO}_2$ . For  $\text{Li-SnO}_2$  and  $\text{Mg-SnO}_2$ , the amount of this part of oxygen species becomes smaller. The variation in the integrated areas of the  $\beta$  peak exhibits a comparable trend, indicating that the surface lattice oxygen of  $\text{Cr-SnO}_2$  and  $\text{Nb-SnO}_2$  becomes also more mobile. However, since most of the surface lattice oxygen releases at much higher temperature, it is believed that the surface facile oxygen could contribute predominantly to the reactions. The amount of the desorbed facile oxygen is sequenced as  $\text{Nb-SnO}_2 > \text{Cr-SnO}_2 > \text{SnO}_2 \approx \text{Zr-SnO}_2 > \text{Mg-SnO}_2 > \text{Li-SnO}_2$ , being consistent with the CO oxidation performance.

### 3.5 In situ DRIFTS investigation of the active surface oxygen sites

To further distinguish the surface-active oxygen types and their reactivity, the representative  $\text{Mg-SnO}_2$  and  $\text{Cr-SnO}_2$  catalysts were studied by *in situ* DRIFTS. The results obtained on the  $\text{Cr-SnO}_2$  catalyst are described in detail here. The sample was initially subjected to a cleaning process at  $500^\circ\text{C}$  in an Ar flow ( $30\text{ mL min}^{-1}$ ) for 60 minutes to ensure surface cleanliness and eliminate the presence of chemisorbed active oxygen that had formed during the initial stages. Subsequently, it was cooled down to  $300^\circ\text{C}$ . The *in situ* cell was then supplied with a stream of  $10\%\text{ O}_2/\text{Ar}$ . Fig. 6(a) displays that compared with the clean catalyst (0 min line), two groups of IR peaks were observed immediately after 1 minute, with one at  $980$ – $1020\text{ cm}^{-1}$  and the other around  $1260\text{ cm}^{-1}$ . The former is assigned to the surface superoxide anions ( $\text{O}_2^-$ ), and the latter is ascribed to the surface oxygen species defined as  $\text{O}^{\delta-}$  ( $0 < \delta < 1$ ).<sup>49,50</sup> After 5 minutes, the two peaks reached a steady state, proving that the surface was fully oxidized by  $\text{O}_2$ . After a duration of

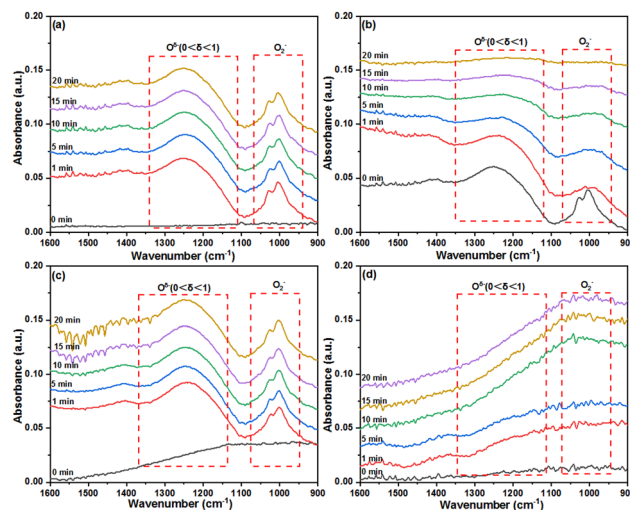


Fig. 6 *In situ* DRIFTS spectra of  $\text{Cr-SnO}_2$  obtained at  $300^\circ\text{C}$  (a) treated in a  $10\%\text{ O}_2/\text{Ar}$  flow, (b) treated in a  $10\%\text{ H}_2/\text{Ar}$  flow and (c) switched back to the  $10\%\text{ O}_2/\text{Ar}$  flow. (d) *In situ* DRIFTS spectra of  $\text{Mg-SnO}_2$  treated in a  $10\%\text{ O}_2/\text{Ar}$  flow at  $300^\circ\text{C}$ .

20 minutes, a feed consisting of  $10\%\text{ H}_2/\text{Ar}$  was introduced into the cell while maintaining the same temperature. The results depicted in Fig. 6(b) demonstrate a fast and complete depletion of both types of surface oxygen anions within 10 minutes, indicating the active and reducible nature of these two oxygen species. After this step, the flow of  $10\%\text{ O}_2/\text{Ar}$  was redirected into the cell while maintaining the same temperature. As shown in Fig. 6(c), the two types of surface oxygen can be fully restored after 10 minutes, even if they are completely consumed by hydrogen.

In contrast, the *in situ* DRIFTS results in Fig. 6(d) obtained with  $\text{Mg-SnO}_2$  exhibit that no any surface  $\text{O}^{\delta-}$  ( $0 < \delta < 1$ ) is present, and the generation of surface  $\text{O}_2^-$  species is also negligible, which explains its poor oxidation activity. In brief, the *in situ* DRIFTS results have substantiated that besides surface  $\text{O}_2^-$  species,  $\text{O}^{\delta-}$  ( $0 < \delta < 1$ ) might be another kind of facile oxygen sites contributing to the reactions for those samples possessing a solid solution structure.

### 3.6 XPS analysis

The surface properties have been analysed using X-ray photoelectron spectroscopy (XPS). Fig. S2 (ESI<sup>†</sup>) presents that two symmetrical peaks were observed around  $487.1$  and  $495.5\text{ eV}$  for all the catalysts, corresponding to  $\text{Sn } 3d_{5/2}$  and  $\text{Sn } 3d_{3/2}$  of  $\text{Sn}^{4+}$ , respectively.<sup>51</sup> The presence of different metal cations is observed to cause a noticeable shift towards lower binding energy regions for the two peaks, indicating that Sn gains electrons from the dopants. The binding-energy gap ( $\Delta E$ ) between the two peaks has been calculated and presented in Table S1 (ESI<sup>†</sup>). In contrast to pure  $\text{SnO}_2$ , all the samples exhibit a slight decrease in  $\Delta E$ , indicating that the chemical environment of lattice  $\text{Sn}^{4+}$  is modified upon doping with metal ions either within the lattice or on the surface.<sup>31</sup> As shown in Fig. S3



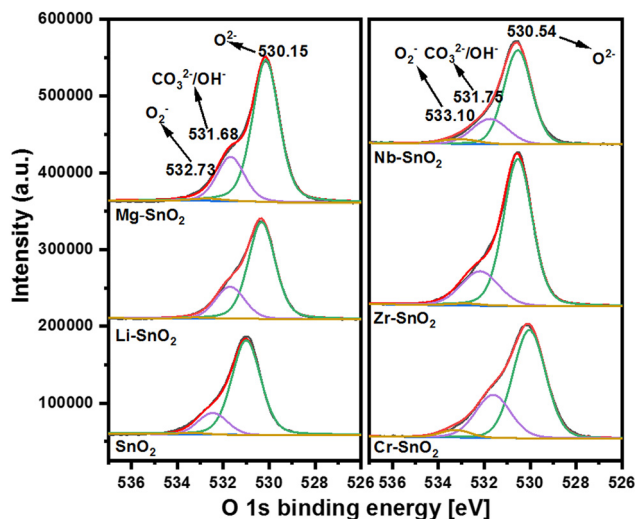


Fig. 7 XPS O 1s spectra of M-SnO<sub>2</sub> catalysts.

(ESI<sup>†</sup>), it has been confirmed that the doping cations are mainly in the states of Li<sup>+</sup>, Mg<sup>2+</sup>, Cr<sup>3+</sup>, Zr<sup>4+</sup> and Nb<sup>5+</sup>, referring to the standard binding energies of the corresponding metal oxides.

The XPS O 1s peaks are thoroughly analysed based on the *in situ* DRIFTS and EPR results. The unsymmetrical O 1s peak, as depicted in Fig. 7, can be fitted into three peaks centered at approximately 530.0, 531.0, and 533.0 eV, corresponding to the surface lattice O<sup>2-</sup>, CO<sub>3</sub><sup>2-</sup>/OH<sup>-</sup> and O<sub>2</sub><sup>-</sup> anchored on the defects of the surface.<sup>52,53</sup> The O<sub>2</sub><sup>-</sup>/O<sup>2-</sup> ratios have been calculated in Table S1 (ESI<sup>†</sup>) to discern the effect of different dopants on the quantity of surface-active oxygen. Interestingly, the ratios are sequenced as Nb-SnO<sub>2</sub> > Cr-SnO<sub>2</sub> > Zr-SnO<sub>2</sub> ≈ SnO<sub>2</sub> > Mg-SnO<sub>2</sub> > Li-SnO<sub>2</sub>, well consistent with the O<sub>2</sub>-TPD and CO oxidation activity order. Nb-SnO<sub>2</sub> and Cr-SnO<sub>2</sub>, the two samples with a solid solution structure, show much higher O<sub>2</sub><sup>-</sup>/O<sup>2-</sup> ratios than pure SnO<sub>2</sub>. In contrast, the doping of Zr<sup>4+</sup> into the SnO<sub>2</sub> lattice improves the O<sub>2</sub><sup>-</sup>/O<sup>2-</sup> ratio only slightly. This seems to imply that doping the SnO<sub>2</sub> lattice with cations having varied valence states (Cr<sup>3+</sup> and Nb<sup>5+</sup>) can create more surface defects than doping with cations having the same valence state (Zr<sup>4+</sup>), thus inducing the creation of a larger amount of surface-active oxygen anions. Notably, Li-SnO<sub>2</sub> and Mg-SnO<sub>2</sub> possess lower O<sub>2</sub><sup>-</sup>/O<sup>2-</sup> ratios than pure SnO<sub>2</sub>, testifying that the Li and Mg nitrates dispersed finely on the surface can suppress surface defects. The observed O<sub>2</sub><sup>-</sup>/O<sup>2-</sup> ratio change achieved *via* XPS is in agreement with the H<sub>2</sub>-TPR, O<sub>2</sub>-TPD, and EPR results, demonstrating consistency with the catalytic activity, especially for CO oxidation.

### 3.7 NH<sub>3</sub>-TPD and propane-TPD studies

As discussed above, for propane deep oxidation, surface acid sites might play a more important role than surface-active oxygen centres. It reported previously that the surface acid sites are very important for the adsorption and activation of the toluene molecule, owing to the delocalized  $\pi^*_o$  bond with rich electrons in its structure, thereby significantly improving the combustion activity.<sup>24,25,54</sup> Therefore, the surface acidity was

Table 4 NH<sub>3</sub>-TPD and propane-TPD quantification results

Sample	NH <sub>3</sub> desorption amount ( $\times 10^{-2}$ mmol g <sup>-1</sup> )	Relative propane desorption amount (a.u.)
SnO <sub>2</sub>	0.74	25.27
Li-SnO <sub>2</sub>	2.01	28.37
Mg-SnO <sub>2</sub>	2.61	30.85
Cr-SnO <sub>2</sub>	5.20	100
Zr-SnO <sub>2</sub>	1.09	23.95
Nb-SnO <sub>2</sub>	3.67	65.87

investigated by conducting NH<sub>3</sub>-TPD experiments. As demonstrated in Fig. S4(a) (ESI<sup>†</sup>), the presence of surface acidic sites is confirmed by the wide NH<sub>3</sub> release peak observed in the range of 50–300 °C for all the catalysts. The calculation results in Table 4 show that the amount of surface acidic sites is ranked as follows: Cr-SnO<sub>2</sub> > Nb-SnO<sub>2</sub> > Mg-SnO<sub>2</sub> > Li-SnO<sub>2</sub> > Zr-SnO<sub>2</sub> > SnO<sub>2</sub>, indicating that doping the metal ions into the SnO<sub>2</sub> lattice to produce solid solutions can generate higher surface acidity. The change trend of the acid site amount is more similar to the propane deep oxidation activity sequence, which seems to indicate that surface acid sites are more important than surface-active oxygen centres for propane oxidation.

The quantification results in Table 4 demonstrate that a solid solution sample with more surface defects generally owns a larger amount of surface acid sites. The previous reports indicated a strong correlation between the quantity of surface Lewis acid sites and surface defects.<sup>29,55,56</sup> Fig. S4(b) (ESI<sup>†</sup>) displays the propane-TPD profiles, and the quantification results in Table 4 prove that the desorption amount of propane follows the same trend, which indicates that the two types of molecules share the same kind of adsorption sites. The relationship between the desorption amount of propane and the number of surface acidic sites is clearly positively correlated, as demonstrated in Fig. 8. Therefore, surface acidity is considered crucial for propane deep oxidation.

### 3.8 The competition of the adsorption sites between NH<sub>3</sub> and propane/CO probed by *in situ* DRIFTS

As supplementary studies, the adsorption of NH<sub>3</sub> and propane on Cr-SnO<sub>2</sub>, the most active catalyst for propane combustion,

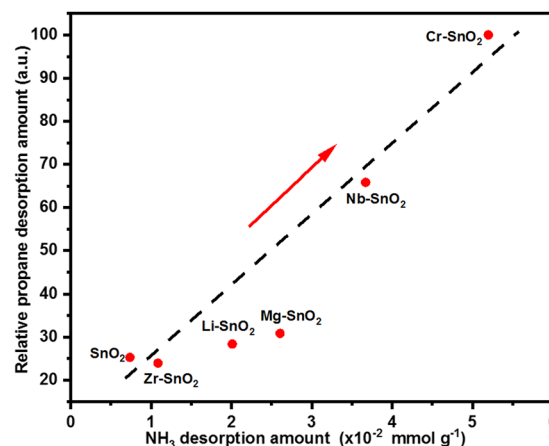


Fig. 8 Propane desorbing amount vs. acidic site amount.

was investigated using *in situ* DRIFTS results as well. The sample was first cleansed at 500 °C in an Ar flow (30 mL min<sup>-1</sup>) for 60 minutes and then cooled down to 50 °C. Fig. 9(a-I) shows that after introducing NH<sub>3</sub>, the range of N-H deformation modes below 1700 cm<sup>-1</sup> exhibited four distinct bands, which can be attributed to the adsorption of NH<sub>3</sub> on various acid sites. The bands at 1622 and 1271 cm<sup>-1</sup> are attributed to NH<sub>3</sub> bound to Lewis-acid sites.<sup>57,58</sup> The bands observed at 1674 and 1450 cm<sup>-1</sup> can be assigned to the presence of NH<sub>3</sub> ions resulting from the protonation of NH<sub>3</sub> on Brønsted acid sites.<sup>57,58</sup> Subsequently, a propane/Ar feed was introduced, and Fig. 9(a-II) does not show any change in the NH<sub>3</sub> adsorbing peaks. This suggests that the propane molecules cannot be adsorbed after the surface acid sites have been occupied by NH<sub>3</sub> molecules. In other words, both the NH<sub>3</sub> and propane molecules could share the same surface acid sites, as testified by the three kinds of TPD experiments in the last section.

To confirm this further, *in situ* DRIFTS experiments by adsorbing NH<sub>3</sub> and propane with a reversed order were also carried out. As shown in Fig. 9(b), after adsorbing propane at 50 °C firstly on the cleansed catalyst, three peaks are observed around 1617, 1454, and 1241 cm<sup>-1</sup>. As labelled in the curves, all of the peaks belong to the dissociative adsorption of propane.<sup>59–61</sup> In addition, a gaseous propane vibration peak is detected around 2968 cm<sup>-1</sup>.<sup>62</sup> After introducing NH<sub>3</sub>, the

three characteristic peaks were replaced by the four typical peaks of adsorbing NH<sub>3</sub>. Therefore, it is strongly proved that both NH<sub>3</sub> and propane are adsorbed on the acidic sites, which are crucial to activate propane molecules.

In addition, CO and NH<sub>3</sub> adsorption was also investigated using the *in situ* DRIFTS technique following the same procedures. Basically, a similar phenomenon is observed in the adsorption of NH<sub>3</sub> and propane. As demonstrated in Fig. 9(c), after the surface of Cr-SnO<sub>2</sub> is pre-saturated by NH<sub>3</sub> molecules, it is difficult to adsorb CO molecules. As shown in Fig. 9(d), after the surface of Cr-SnO<sub>2</sub> is pre-saturated by CO molecules again, NH<sub>3</sub> molecules can drive out the pre-adsorbed CO molecules. Since a CO molecule contains  $\pi$ -back bonding, surface acid sites are necessary for its adsorption/activation. But the surface-active oxygen sites may play a more critical role than the surface acid sites for CO oxidation, as discussed above.

### 3.9 The reaction intermediates probed by *in situ* DRIFTS

The possible pathway of propane oxidation was investigated through a series of *in situ* DRIFTS experiments carried out on Cr-SnO<sub>2</sub>, recognized as the most active catalyst for this reaction in this work.

The first series: the sample was initially subjected to a purification process at 500 °C in an Ar flow (30 mL min<sup>-1</sup>) for 60 minutes, followed by a decrease in temperature to 50 °C.

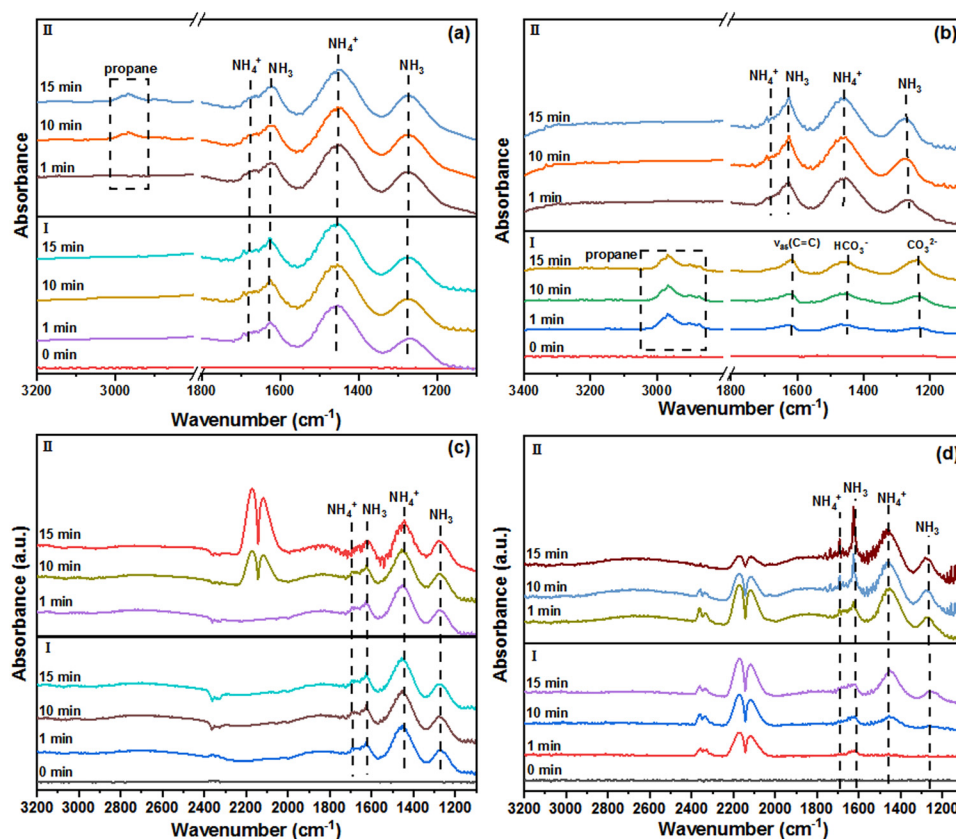


Fig. 9 *In situ* DRIFT adsorption spectra of Cr-SnO<sub>2</sub> at 50 °C, (a-I) treated in a NH<sub>3</sub>/Ar stream, (a-II) treated in a propane/Ar stream, (b-I) treated in a propane/Ar stream, (b-II) treated in a NH<sub>3</sub>/Ar stream, (c-I) treated in a NH<sub>3</sub>/Ar stream, (c-II) treated in a CO/Ar stream, (d-I) treated in a CO/Ar stream, (d-II) treated in a NH<sub>3</sub>/Ar stream.



Subsequently, a propane feed mixed with Ar was directed into the cell in the temperature range of 50–300 °C. As shown in Fig. 10(a), at 50 and 100 °C, the surface adsorption of propane is very weak, and gas phase propane is obviously detected at 2968 and 2982 cm<sup>-1</sup>. However, after the temperature is increased to 200 °C, the initially very weak adsorption peaks can be evidently detected. The peaks observed at 2902 and 2876 cm<sup>-1</sup> can be attributed to the C-H vibrations of CH, CH<sub>2</sub>, or CH<sub>3</sub> species, suggesting that propane undergoes adsorption, partial oxidation, and cracking on the catalyst surface.<sup>63</sup> At 50 °C, the peak at 1620 cm<sup>-1</sup> is assigned to the vibration of the C=C bond. When the temperature was increased to 100 °C, it was oxidized to form C=O bonds detected at 1676 cm<sup>-1</sup>.<sup>64</sup> When the temperature is higher than 200 °C, new bands appeared at 1542, 1384, 1351, and 1424 cm<sup>-1</sup>, which are assigned to  $\nu_{\text{as}}$  (COO),  $\delta_{\text{s}}$  (CH<sub>3</sub>), O–C–O bonds in carboxylate species and carbonate species, respectively.<sup>64,65</sup> The evidence exhibits that the presence of surface O<sup>2-</sup> species facilitates the partial oxidation of propane adsorbed on the catalyst. As shown in Fig. S5(a) (ESI<sup>†</sup>), compared with Cr–SnO<sub>2</sub>, the formation of those intermediate species is not observed on Mg–SnO<sub>2</sub>, showing that propane cannot be sufficiently activated under the same condition. However, Fig. S5(b) (ESI<sup>†</sup>) indicates that much weaker intermediate peaks can still be detected on Nb–SnO<sub>2</sub>, which indicates that propane can only be mildly activated.

The second series: as displayed in Fig. 10(b-I), full adsorption of propane was carried out at 300 °C to generate the intermediates detected in the first series of experiments. After this, 10% O<sub>2</sub>/Ar was introduced at the same temperature. As shown in Fig. 10(b-II), the intermediate bands exhibited a quick decrease, particularly those in relation to the oxygenates. This observation provides evidence that these adsorption species may serve as reactive intermediates during propane combustion.

The third series: a batch of fresh catalysts was subjected to the same pretreatment process as in the first series of experiments for surface cleansing, followed by temperature controlling at 300 °C. After being fully oxidized in a 10% O<sub>2</sub>/Ar feed, Fig. 10(c-I) shows that two groups of peaks around 1000 and 1200 cm<sup>-1</sup> appear, corresponding to O<sub>2</sub><sup>-</sup> and O<sup>δ-</sup> in a sequence. Afterwards, a propane/Ar stream was switched into the cell. Fig. 10(c-II) shows that the O<sup>δ-</sup> sites are used up after 15 minutes but some O<sub>2</sub><sup>-</sup> species remain, implying that the former is more active than the latter. At the same time, the detection of the intermediates observed in the initial series of experiments occurs. This suggests that both O<sup>δ-</sup> and O<sub>2</sub><sup>-</sup> sites serve as active centres for propane oxidation, potentially exhibiting higher reactivity compared to the surface lattice O<sup>2-</sup>.

The fourth series: after cleansing the catalyst, the reaction flow consisting of 5000 ppm propane + 10% O<sub>2</sub>/Ar was introduced into the cell at 300 °C. As shown in Fig. 10(d), after 5 minutes, the formation of the intermediates is obviously

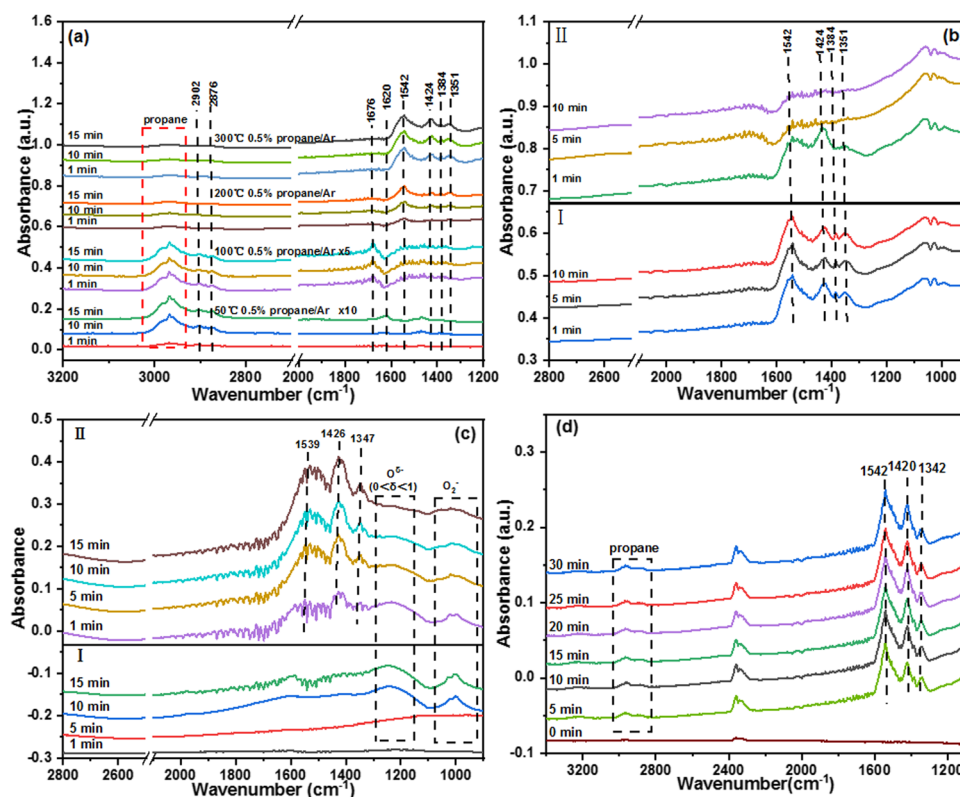


Fig. 10 *In situ* DRIFTS experiments on Cr–SnO<sub>2</sub>, (a) exposed in propane/Ar flow under different situations, (b-I) exposed in propane/Ar flow at 300 °C, (b-II) exposed in 10% O<sub>2</sub>/Ar flow at 300 °C, (c-I) exposed in a 10% O<sub>2</sub>/Ar flow at 300 °C, (c-II) exposed in propane/Ar flow at 300 °C, (d) exposed in the reaction feed consisting of 5000 ppm propane/Ar + 10% O<sub>2</sub>/Ar.

detected as well. In contrast, as shown in Fig. S5(a') and (b') (ESI†), the formation of the above intermediates on Mg-SnO<sub>2</sub> and Nb-SnO<sub>2</sub> is marginal under the same conditions, exhibiting that during the reaction process, propane molecules can only be mildly activated. Different from the second series of experiments, with the co-existence of propane and gaseous O<sub>2</sub>, these intermediates are always detected. This strongly demonstrates that these surface species are the reaction intermediates for propane combustion, which can be formed, consumed, regenerated, and can reach equilibrium quickly under real reaction conditions with gas phase O<sub>2</sub>.

Based on the *in situ* DRIFTS results, a possible pathway, propane → propene → acrylaldehyde → acrylic acid → acrylate → CO<sub>3</sub><sup>2-</sup> → CO<sub>2</sub>, is illustrated in Scheme 1.<sup>59,60,64</sup> The adsorption of propane molecules on the Cr-SnO<sub>2</sub> surface is proposed to be converted into different intermediates, including propylene, acrolein, carboxylate, carbonate species and others. Both the adsorbed O<sup>δ-</sup>/O<sub>2</sub><sup>-</sup> species and lattice O<sup>2-</sup> could be involved in the intermediate formation process, but the O<sup>δ-</sup>/O<sub>2</sub><sup>-</sup> anions can react more effectually with the intermediates to produce H<sub>2</sub>O and CO<sub>2</sub>.

### 3.10 Stability and tolerance tests for sulfur and/or water vapor

The reaction stability and sulphur and water resistance of Cr-SnO<sub>2</sub>, the most active catalyst for propane combustion, have been tested at 320 °C. Fig. S6(a) (ESI†) shows that the propane conversion is steady in a dry feed during 50 hours' running. In addition, Fig. S6(b) (ESI†) exhibits that in 5% water vapor, the overall activity exhibits only a mild decrease but can be fully restored after removing water. Interestingly, adding only 10 ppm SO<sub>2</sub> in the flow has no negative impact on the activity, whereas adding 5% water vapor and 10 ppm SO<sub>2</sub> together can obviously degrade the activity, as evidenced by the decreased propane conversion. Furthermore, the deactivation cannot be restored completely after stopping the two poisoning agents.

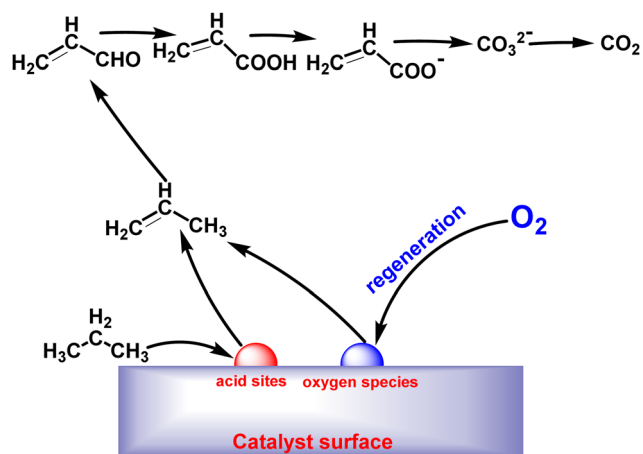
Therefore, Raman spectroscopy, FTIR spectroscopy and H<sub>2</sub>-TPR techniques have been used to elucidate the reasons. In comparison with the fresh catalyst, Fig. S7(a) (ESI†) exhibits

that the characteristic Raman bands of SnO<sub>2</sub> phases disappeared on the partly deactivated catalyst, indicating that its surface composition has been changed. As exhibited in Fig. S7(b) (ESI†), a sulphate peak at 1000 cm<sup>-1</sup> is observed obviously *via* FTIR spectroscopy. Additionally, the H<sub>2</sub>-TPR results in Fig. S7(c) (ESI†) have proven that the low temperature reducing peak belonging to the surface facile oxygen nearly disappears. This strongly shows that when water vapor and sulphur oxide are co-fed into the reaction flow, some stable surface sulphates are generated, which can damage the surface-active oxygen centres, thus being harmful to the catalytic reactivity.

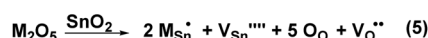
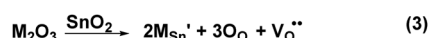
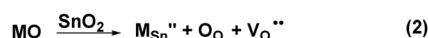
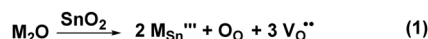
## 4. A short discussion

In this work, aiming to understand the effects of doping cations with different valence states on the structure–reactivity of solid solution catalysts, five metal ions (Li<sup>+</sup>, Mg<sup>2+</sup>, Cr<sup>3+</sup>, Zr<sup>4+</sup> and Nb<sup>5+</sup>) with radii similar to Sn<sup>4+</sup> (CN = 6) have been selected to modify SnO<sub>2</sub>. As an endeavour to incorporate these cations into the lattice matrix of tetragonal SnO<sub>2</sub>, a sol–gel method was employed to synthesize the catalysts. It was confirmed *via* XPS that the doping ions are present as Li<sup>+</sup>, Mg<sup>2+</sup>, Cr<sup>3+</sup>, Zr<sup>4+</sup> and Nb<sup>5+</sup> on/in the catalysts. XRD and Raman results have proven that Cr<sup>3+</sup>, Zr<sup>4+</sup> and Nb<sup>5+</sup> have successfully been doped into the lattice of SnO<sub>2</sub> to substitute part of the Sn<sup>4+</sup> to generate solid solutions. As shown in the following equations (1–5), the incorporated ions (Cr<sup>3+</sup>, Zr<sup>4+</sup> and Nb<sup>5+</sup>) typically differ from Sn<sup>4+</sup> in terms of radius and/or valence state, hence resulting in charge imbalance, lattice distortion, and defects in the obtained solid solution. This ultimately enhances the diffusion rate of bulk phase oxygen and forms more oxygen vacancies/defects.

In turn, these defects/vacancies can promote the generation of a higher concentration of surface-active oxygen species (O<sup>δ-</sup> and O<sub>2</sub><sup>-</sup>), which are favourable to CO oxidation and propane combustion.<sup>66–69</sup> It is also discovered that for the three solid solution catalysts, if the doping cations (Cr<sup>3+</sup> and Nb<sup>5+</sup>) have more varied valence states than Sn<sup>4+</sup>, there is a higher formation of surface defects than Zr<sup>4+</sup> having the same valence state. Therefore, Nb-SnO<sub>2</sub> and Cr-SnO<sub>2</sub> possess a higher concentration of surface-active oxygen sites than Zr-SnO<sub>2</sub>, displaying better oxidation activity.



Scheme 1 Proposed pathway for propane oxidation on Cr-SnO<sub>2</sub> catalysts.



However, although Li<sup>+</sup> and Mg<sup>2+</sup> have radii similar to Sn<sup>4+</sup> at CN = 6, their valence state deviation is too big to form a solid solution structure, thus Li and Mg nitrates are present on the catalyst surfaces, which can cover and suppress the surface

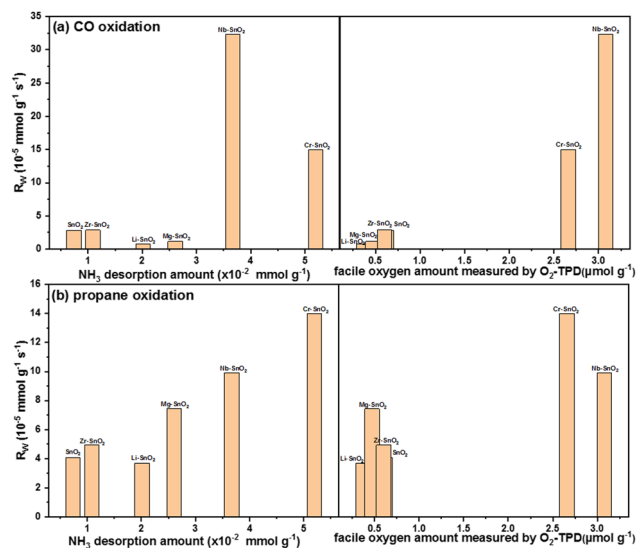


Fig. 11 (a) CO oxidation rates versus facile oxygen amount and  $\text{NH}_3$  desorption amount; (b) propane oxidation rates versus facile oxygen amount and  $\text{NH}_3$  desorption amount.

defects/vacancies of  $\text{SnO}_2$ . As a result,  $\text{Li-SnO}_2$  and  $\text{Mg-SnO}_2$  exhibit lower oxidation activity than individual  $\text{SnO}_2$ .

Most interestingly, though the concerted interaction between surface active oxygen and acidic sites is important for CO oxidation and propane oxidation, the two kinds of active sites have different weights in the two reactions. Fig. 11(a) displays that the activity of CO oxidation is almost positively correlated to the surface-active oxygen amount but not to the surface acid site amount. This indicates that the surface facile oxygen is more effective for CO oxidation than the surface acidity. However, Fig. 11(b) shows that the propane combustion activity is nearly proportional to the quantity of surface acid sites but not to the quantity of surface-active oxygen sites. This testifies that different from the case of CO oxidation, surface acid sites could play a more crucial role than the active oxygen species for propane combustion.

## 5. Conclusion

Targeting to unravel the valence state influence of doping cations on the structure-reactivity of solid solution catalysts, a series of metal ions ( $\text{Li}^+$ ,  $\text{Mg}^{2+}$ ,  $\text{Cr}^{3+}$ ,  $\text{Zr}^{4+}$  and  $\text{Nb}^{5+}$ ) with radii similar to  $\text{Sn}^{4+}$  ( $\text{CN} = 6$ ) but with varied valence states have been adopted to dope  $\text{SnO}_2$ . The prepared catalysts have been characterized using multiple techniques and evaluated by CO and propane oxidation.

(1) XRD and Raman results have proven that  $\text{Cr}^{3+}$ ,  $\text{Zr}^{4+}$ , and  $\text{Nb}^{5+}$  can be successfully incorporated into the matrix of  $\text{SnO}_2$  to substitute part of the  $\text{Sn}^{4+}$  to form solid solutions, which results in more abundant surface defects. In contrast, due to too big deviation of the valence state from  $\text{Sn}^{4+}$ ,  $\text{Li}^+$  and  $\text{Mg}^{2+}$  cannot enter the lattice of  $\text{SnO}_2$  but can mainly be present in the form of nitrates on the catalyst surfaces, thus suppressing the surface defects.

(2) The abundant surface defect on the solid solution catalysts promotes the generation of both active surface oxygen ( $\text{O}_2^-$  and  $\text{O}^{\delta-}$ ) and acid sites, thus improving catalytic performance. It is concluded that the active oxygen sites play a more critical role than the acid sites for CO oxidation. In contrast, the surface acid sites play a more crucial role than the active oxygen sites for propane combustion.

(3) On the active  $\text{Cr-SnO}_2$  for propane oxidation, reactive intermediates such as adsorbed propylene, acrylaldehyde, carboxylate *etc.* can be formed effectively. However, on those catalysts with low activity, the formation of these intermediates is negligible.

## Author contributions

Haiming Yan: data curation, formal analysis, investigation, methodology, software, writing – original draft. Teng Liu: data curation, formal analysis, investigation, validation, writing – original draft. Yu Lv: data curation, investigation, validation. Xianglan Xu: data curation, investigation, methodology. Junwei Xu: data curation; investigation; methodology. Xiuzhong Fang: data curation, investigation, methodology. Xiang Wang: conceptualization, funding acquisition, investigation, methodology, project administration, resources, supervision, validation, writing – review & editing.

## Conflicts of interest

There are no conflicts to declare.

## Acknowledgements

The authors sincerely acknowledge the financial support provided by the National Natural Science Foundation of China (22376090, 22172071, and 21962009) and the Natural Science Foundation of Jiangxi Province (20224BAB213017).

## References

- 1 Z. Wang, Y. Liu, T. Yang, J. Deng, S. Xie and H. Dai, *Chin. J. Catal.*, 2017, **38**, 207–216.
- 2 C. He, J. Cheng, X. Zhang, M. Douthwaite, S. Patisson and Z. Hao, *Chem. Rev.*, 2019, **119**, 4471–4568.
- 3 J. Chen, X. Guo, L. Lang, X. Yin, A. Wang and Z. Rui, *Appl. Surf. Sci.*, 2023, **618**, 153275.
- 4 M. Ousmane, L. F. Liotta, G. Pantaleo, A. M. Venezia, G. Di Carlo, M. Aouine, L. Retailleau and A. Giroir-Fendler, *Catal. Today*, 2011, **176**, 7–13.
- 5 H. Huang, Y. Xu, Q. Feng and D. Y. C. Leung, *Catal. Sci. Technol.*, 2015, **5**, 2649–2669.
- 6 K. Yang, Y. Liu, J. Deng, X. Zhao, J. Yang, Z. Han, Z. Hou and H. Dai, *Appl. Catal., B*, 2019, **244**, 650–659.
- 7 Y. Guo, M. Wen, G. Li and T. An, *Appl. Catal., B*, 2021, **281**, 119447.



- 8 K. Zeng, Y. Wang, C. Huang, H. Liu, X. Liu, Z. Wang, J. Yu and C. Zhang, *Ind. Eng. Chem. Res.*, 2021, **60**, 6111–6120.
- 9 X. Ma, Y. Tang, Y. Liu, Y. Zhang, L. Jia, X. Liu, C. Du and B. Shan, *J. Catal.*, 2022, **409**, 59–69.
- 10 L. F. Liotta, *Appl. Catal., B*, 2010, **100**, 403–412.
- 11 Q. Zhang, S. Mo, J. Li, Y. Sun, M. Zhang, P. Chen, M. Fu, J. Wu, L. Chen and D. Ye, *Catal. Sci. Technol.*, 2019, **9**, 4538–4551.
- 12 T. F. Garetto, E. Rincón and C. R. Apesteguía, *Appl. Catal., B*, 2004, **48**, 167–174.
- 13 A. Hinz, M. Skoglundh, E. Fridell and A. Andersson, *J. Catal.*, 2001, **201**, 247–257.
- 14 Z. Hu, Z. Wang, Y. Guo, L. Wang, Y. Guo, J. Zhang and W. Zhan, *Environ. Sci. Technol.*, 2018, **52**, 9531–9541.
- 15 R. Peng, S. Li, X. Sun, Q. Ren, L. Chen, M. Fu, J. Wu and D. Ye, *Appl. Catal., B*, 2018, **220**, 462–470.
- 16 M. S. Kamal, S. A. Razzak and M. M. Hossain, *Atmos. Environ.*, 2016, **140**, 117–134.
- 17 L. Chen, J. Ding, J. Jia, R. Ran, C. Zhang and X. Song, *ACS Appl. Nano Mater.*, 2019, **2**, 4417–4426.
- 18 C. Feng, Q. Gao, G. Xiong, Y. Chen, Y. Pan, Z. Fei, Y. Li, Y. Lu, C. Liu and Y. Liu, *Appl. Catal., B*, 2022, **304**, 121005.
- 19 G. Li, N. Li, Y. Sun, Y. Qu, Z. Jiang, Z. Zhao, Z. Zhang, J. Cheng and Z. Hao, *Appl. Catal., B*, 2021, **282**, 119512.
- 20 C.-F. Liu, L.-C. He, X.-F. Wang, J. Chen, J.-Q. Lu and M.-F. Luo, *Mol. Catal.*, 2022, **524**, 112297.
- 21 S. Das and V. Jayaraman, *Prog. Mater. Sci.*, 2014, **66**, 112–255.
- 22 X. Kang, N. Deng, Z. Yan, Y. Pan, W. Sun and Y. Zhang, *Mater. Sci. Semicond. Process.*, 2022, **138**, 106246.
- 23 L. Villamagua, A. Stashans, P.-M. Lee, Y.-S. Liu, C.-Y. Liu and M. Carini, *Chem. Phys.*, 2015, **452**, 71–77.
- 24 Y. Guo, J. Liang, Y. Liu, Y. Liu, X. Xu, X. Fang, W. Zhong and X. Wang, *Ind. Eng. Chem. Res.*, 2019, **58**, 18569–18581.
- 25 Y. Guo, L. Zeng, X. Xu, Y. Liu, Y. Liu, X. Fu, Z. Gao, Z. Qian, J. Xu, X. Fang and X. Wang, *Appl. Catal., A*, 2020, **605**, 117755.
- 26 N. Kamiuchi, H. Muroyama, T. Matsui, R. Kikuchi and K. Eguchi, *Appl. Catal., A*, 2010, **379**, 148–154.
- 27 M. A. Mäki-Jaskari and T. T. Rantala, *Phys. Rev. B: Condens. Matter Mater. Phys.*, 2002, **65**, 1–8.
- 28 R. Sasikala, N. M. Gupta and S. K. Kulshreshtha, *Catal. Lett.*, 2001, **71**, 69–73.
- 29 J. Zhang, Y. Liu, Y. Sun, H. Peng, X. Xu, X. Fang, W. Liu, J. Liu and X. Wang, *Ind. Eng. Chem. Res.*, 2018, **57**, 10315–10326.
- 30 X. L. Xu, Y. Y. Tong, J. Y. Zhang, X. Z. Fang, J. W. Xu, F. Y. Liu, J. J. Liu, W. Zhong, O. E. Lebedeva and X. Wang, *Chin. J. Catal.*, 2020, **41**, 877–888.
- 31 X. L. Xu, F. Liu, X. Han, Y. Y. Wu, W. M. Liu, R. B. Zhang, N. Zhang and X. Wang, *Catal. Sci. Technol.*, 2016, **6**, 5280–5291.
- 32 X. Wang and Y. C. Xie, *Catal. Lett.*, 2001, **75**, 73–80.
- 33 X. Wang and Y. C. Xie, *Appl. Catal., B*, 2001, **35**, 85–94.
- 34 X. Yao, C. Tang, Z. Ji, Y. Dai, Y. Cao, F. Gao, L. Dong and Y. Chen, *Catal. Sci. Technol.*, 2013, **3**, 688–698.
- 35 Y. Zhang, Y. J. Zhou, J. P. Lin, G. L. Chen and P. K. Liaw, *Adv. Eng. Mater.*, 2008, **10**, 534–538.
- 36 A. R. Denton and N. W. Ashcroft, *Phys. Rev. A*, 1991, **43**, 3161–3164.
- 37 X. Feng, S. Zhang, R. Liu, J. Ma, X. Xu, J. Xu, X. Fang and X. Wang, *Phys. Chem. Chem. Phys.*, 2022, **24**, 3250–3258.
- 38 M. Balamurugan, R. Shanmugam, T.-W. Chen, S.-M. Chen, B.-S. Lou, X. Liu and C.-Y. Hong, *Food Chem.*, 2021, **361**, 130162.
- 39 Q. Sun, X. Xu, H. Peng, X. Fang, W. Liu, J. Ying, F. Yu and X. Wang, *Chin. J. Catal.*, 2016, **37**, 1293–1302.
- 40 Y.-C. Xie and Y.-Q. Tang, *Adv. Catal.*, Academic Press, 1990, vol. 37, pp. 1–43.
- 41 R. Zhang, X. Liu, H. Liang, X. Yang, J. Li, W. Ye, X. Wang and B. Liu, *RSC Adv.*, 2022, **12**, 26238–26244.
- 42 Z. Qu, M. Cheng, W. Huang and X. Bao, *J. Catal.*, 2005, **229**, 446–458.
- 43 Q. Zou, Y. Zhao, X. Jin, J. Fang, D. Li, K. Li, J. Lu and Y. Luo, *Appl. Surf. Sci.*, 2019, **494**, 1166–1176.
- 44 P. Venkataswamy, K. N. Rao, D. Jampaiah and B. M. Reddy, *Appl. Catal., B*, 2015, **162**, 122–132.
- 45 T. Li, G. Xiang, J. Zhuang and X. Wang, *Chem. Commun.*, 2011, **47**, 6060–6062.
- 46 Y. Gu, S. Shao, W. Sun, H. Xia, X. Gao, Q. Dai, W. Zhan and X. Wang, *J. Catal.*, 2019, **380**, 375–386.
- 47 X. Li, L. Zhang, Z. Yang, P. Wang, Y. Yan and J. Ran, *Sep. Purif. Technol.*, 2020, **235**, 116213.
- 48 A. Gurlo, *ChemPhysChem*, 2006, **7**, 2041–2052.
- 49 J. Liu, L. Zeng, X. Xu, J. Xu, X. Fang, Y. Bian and X. Wang, *ChemCatChem*, 2022, **14**, e2021019.
- 50 H. L. Wan, Z. S. Chao, W. Z. Weng, X. P. Zhou, J. X. Cai and K. R. Tsai, *Catal. Today*, 1996, **30**, 67–76.
- 51 B. Babu, I. N. Reddy, K. Yoo, D. Kim and J. Shim, *Mater. Lett.*, 2018, **221**, 211–215.
- 52 E. McCafferty and J. P. Wightman, *Surf. Interface Anal.*, 1998, **26**, 549–564.
- 53 V. J. Ferreira, P. Tavares, J. L. Figueiredo and J. L. Faria, *Catal. Commun.*, 2013, **42**, 50–53.
- 54 D. Farmanzadeh and A. Valipour, *Appl. Surf. Sci.*, 2018, **450**, 509–515.
- 55 J. Sun, Y. Lu, L. Zhang, C. Ge, C. Tang, H. Wan and L. Dong, *Ind. Eng. Chem. Res.*, 2017, **56**, 12101–12110.
- 56 H. Wang, Z. Qu, H. Xie, N. Maeda, L. Miao and Z. Wang, *J. Catal.*, 2016, **338**, 56–67.
- 57 J. Xu, B. Mojet, J. Vanommen and L. Lefferts, *J. Catal.*, 2005, **232**, 411–423.
- 58 J. Wang, Z. Yan, L. Liu, Y. Chen, Z. Zhang and X. Wang, *Appl. Surf. Sci.*, 2014, **313**, 660–669.
- 59 B. Wang, X. Wu, R. Ran, Z. Si and D. Weng, *J. Mol. Catal. A: Chem.*, 2012, **361–362**, 98–103.
- 60 B. Wang, X. Wu, R. Ran, Z. Si and D. Weng, *J. Mol. Catal. A: Chem.*, 2012, **356**, 100–105.
- 61 M. I. Z. M. A. Hasan and L. Pasupulety, *J. Phys. Chem. B*, 2002, **106**, 12747–12756.
- 62 D. D. Li, X.-Y. Leng, X.-F. Wang, H.-B. Yu, W.-Q. Zhang, J. Chen, J.-Q. Lu and M.-F. Luo, *J. Catal.*, 2022, **407**, 322–332.
- 63 W. L. S. Faria, C. A. C. Perez, D. V. César, L. C. Dieguez and M. Schmal, *Appl. Catal., B*, 2009, **92**, 217–224.

- 64 J. Wu, B. Chen, J. Yan, X. Zheng, X. Wang, W. Deng and Q. Dai, *Chem. Eng. J.*, 2022, **438**, 135501.
- 65 L. Cano-Casanova, B. Mei, G. Mul, M. A. Lillo-Rodenas and M. D. C. Roman-Martinez, *Nanomaterials*, 2020, **10**, 1314.
- 66 Z. Hu, B. Li, X. Sun and H. Metiu, *J. Phys. Chem. C*, 2011, **115**, 3065–3074.
- 67 M. D. Krcha, A. D. Mayernick and M. J. Janik, *J. Catal.*, 2012, **293**, 103–115.
- 68 A. P. Pushkar and J. J. Varghese, *J. Catal.*, 2022, **413**, 681–691.
- 69 X. Sun, B. Li and H. Metiu, *J. Phys. Chem. C*, 2013, **117**, 23597–23608.